Location of quantum dots identified by microscopic photoluminescence changes during nanoprobe indentation with a horizontal scan

Yuan-Hua Liang, Masane Ohashi, and Yoshio Arai*
Graduate School of Science and Engineering, Saitama University, 255 Shimo-Ohkubo, Sakura-ku, Saitama 338-0825, Japan

Kazunari Ozasa
RIKEN (The Institute of Physical and Chemical Research), 2-1 Hirosawa, Wako, Saitama 351-0198, Japan
(Received 22 December 2006; revised manuscript received 15 March 2007; published 15 May 2007)

The location of quantum dots (QDs) embedded in a GaAs matrix is successfully identified by microscopic photoluminescence (PL) measurement during nanoprobe indentation with a horizontal scan at low temperature (10 K). By introducing a high-sensitive load cell and a focused ion beam-fabricated flat-apex nanoprobe, the indentation force and PL of QDs are measured simultaneously at each point in the direction of the nanoprobe horizontal scanning with a constant indentation force. The experimental results show that the emission energy from QDs has a strong dependence on the location of QDs relative to the nanoprobe-indented location. Consequently, the emission energy shifts with the nanoprobe scan, generating an emission trace with a constant indentation force. Based on the energy shift of the ground state of the QD simulated by the combination of three-dimensional finite element strain calculation and strain-dependent $\mathbf{k}\cdot\mathbf{p}$ Hamiltonian, an estimation method is developed, which enables us to identify the location of the QD from its emission trace in the nanoprobe indentation experiment. Results indicate that all the emission traces clearly observed are emitted from the QDs around the edge of the nanoprobe-indented area. Further discussion reveals that the evolution of shear strain generates hole accumulation around the contact edge of the indented nanoprobe. Consequently, the high density of holes enhances the PL of the QDs in that region.

DOI: 10.1103/PhysRevB.75.195318 PACS number(s): 73.21.La, 78.55.−m, 78.55.Cr

I. INTRODUCTION

In(Ga)As/GaAs quantum dots (QDs) have extensive promising applications in electronic and optoelectronic devices, such as semiconductor lasers,[1–3] light-emitting diodes,[4–6] single electron transistors,[7] infrared detectors,[8,9] and quantum communications.[10] To improve the performance of QD-based devices, it is crucial to gain detailed understanding on the optical and electronic structure of quantum dots and their control. It is also significant to measure the mechanical, optical, and electrical properties of individual QDs. This involves knowledge on three fronts: location of the QD, strain experienced by the QD, and response of the QD. For the location of the QD, various methods had been employed to describe the conformation of the QD sample, such as scanning electron microscope,[11,12] scanning tunneling microscope,[13,14] atomic force microscope,[11,12] and surface-sensitive grazing incidence x-ray diffraction.[15] For the strain-based modulation of the QD, much work has been done to tune the discrete energy levels of QDs by thermal annealing,[16] strain-release capping layer,[17] hydrostatic pressure by diamond-anvil cell,[18] and local indentation by nanoprobe.[19–26] For response measurement of the QD, a widely used method was spectroscopy.[18–26] However, only a few experiments have tried to combine mechanical manipulation and optical spectroscopy; for example, the diamond-anvil cell only measures the energy shift of the whole QD sample due to the external hydrostatic pressure.[18] The indentation of the optical fiber nanoprobe provides an efficient way to exert local pressure on the QD sample and to measure the photoluminescence (PL) of the QDs near the aperture of the probe,[19–26] but no effort has been made to identify the locations of the observed QDs in these studies.[19–26] Furthermore, the quantitative understanding of the dependence of the energy-level shifts of QDs on the external strain has been insufficient to realize the precise tuning of the energy levels of QDs in most of the above-mentioned works.[19–25] This is because the shapes of the probes were not fabricated precisely,[19–24] or the two-dimensional analysis was insufficient to describe the three-dimensional (3D) strain field of the QD.[19,20,23–25] Additionally, the indentation force in these experiments was estimated indirectly from the displacement at the end of nanoprobe connected to the piezo-unit.[19–25] A system that can realize the addressing, tuning, and response measurement of individual QDs is required for a better understanding of the electronic and optical properties of individual QDs.

In this paper, a method of location identification of QDs based on the combination of nanoprobe indentation system and high-sensitive load cell is developed to realize the addressing, tuning, and PL measurement of individual QDs. First, based on the simultaneous measurement of the indentation force and PL of QDs achieved by introducing a sensitive load cell into a nanoprobe indentation system,[26] the PL spectrum of the QDs is measured at each point in the direction of the nanoprobe horizontal scanning with a constant indentation force. Second, a theoretical analysis is performed through a three-dimensional finite element (FE) calculation and six-band strain-dependent Hamiltonian. Finally, the locations of the QDs relative to the nanoprobe are determined from fitting of PL peak energy shifts with the horizontal scan. PL enhancement due to strain-induced hole accumulation is also discussed.

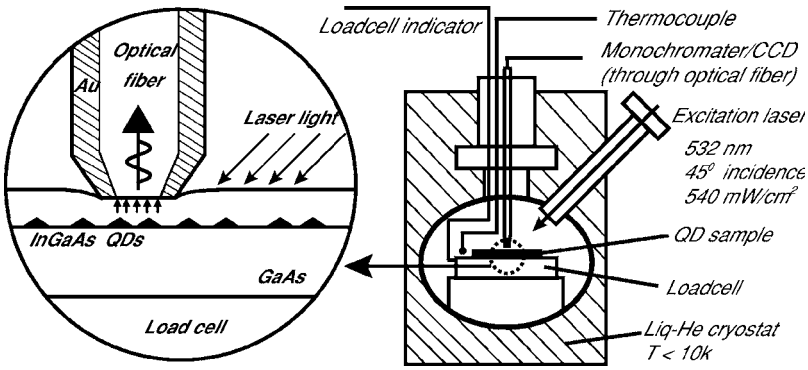

FIG. 1. Sketch of the experimental setup.

II. EXPERIMENT

The sample of $In_{0.5}Ga_{0.5}As$ QDs was prepared on a (001) GaAs substrate by chemical beam epitaxy.[27,28] Next, the QDs were capped with a 50 nm thick GaAs layer. The configuration for the nanoprobe PL measurement is given schematically in Fig. 1. A solid-state laser (532 nm and 540 mW/cm^2) was used to excite photocarriers in GaAs with an incidence angle of 45°. The apex of Au-coated nanoprobe was cut by focused ion beam (FIB) to obtain a flat top surface with an aperture of 850 nm in diameter. The nanoprobe was used to apply indentation force on the QD sample, and at the same time to collect the PL of the sample through its aperture. The indentation force was measured by a cylindrical load cell of the resistance-bridge type (Tokyo Sokki Kenkyujo). The PL collected by the nanoprobe was analyzed in a monochromater (SPEX, 270M) and a charge coupled device (CCD) detector (SPEX, CCD-2000). With this apparatus, the simultaneous measurement of indentation force and PL of QDs was successfully achieved.[26] In the experiments described in this paper, a series of the measurements was performed as follows: one PL spectrum from the QDs was measured at the location where the nanoprobe was pressed onto the sample with a fixed force of 1.3 mN. The force was measured directly by the high-sensitive load cell. After the acquisition of one PL spectrum, the probe was lifted up to the load-free state, moved horizontally by 6.6 nm, and pressed on the sample with the same force again for the next PL spectrum measurement. This sequence was repeated 287 times, which corresponds to a scanning distance of more than 1.8 μm. In the scan experiments, the PL enhancement was found with the indentation force ranging from 0.5 to at least 1.5 mN. The indentation force of 1.3 mN was adopted as a typical one because the emission traces were clearly resolved at the force. Other forces were also examined in the similar experiments. It was found that almost the same results were obtained from the viewpoint of QD location identification. The dependence of the energy shifts on different indentation forces and scanning will be discussed in detail in the future work.

Figure 2 shows the dependence of the emission energy of QDs obtained with the horizontal movement of the probe as described above. A vertical slice of this figure contains the PL spectrum for a given location of probe under a constant force. The brightness in Fig. 2 corresponds to the PL intensity. The bright streaks (traces) show the shift of the emission energy of individual QDs due to the nanoprobe indentation with the horizontal scan. By tracing the typical bright streaks in Fig. 2(a), the shifts of the emission energy of the representative QDs are obtained, as shown in Fig. 2(b). It can be seen from Fig. 2(b) that the emission energy of QDs has a strong dependence on the indented location of the nanoprobe, which is in agreement with our previous results.[26] The different shapes in the traces of the emission energy of QDs indicate the different locations of QDs relative to the nanoprobe, which will be used to identify the location of the QD in Sec. IV. It is also impressive that the vast majority of the emission lines in Fig. 2 has positive slope, which indicates that the corresponding dots are positioned in front of the

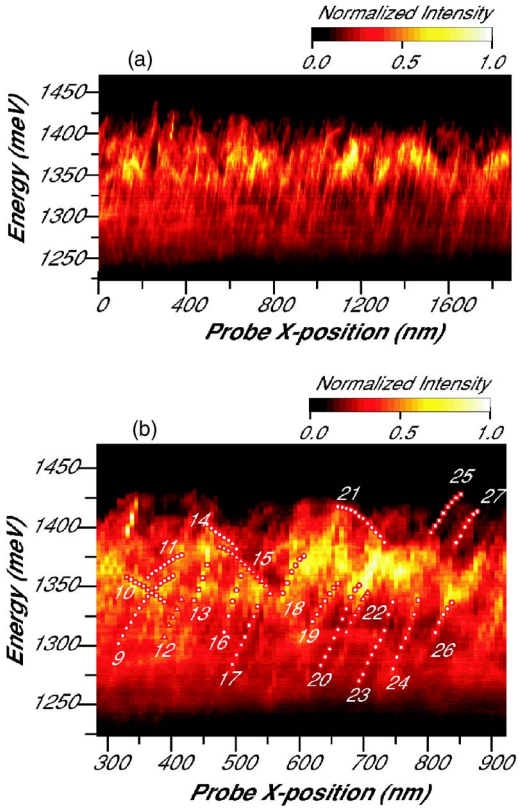

FIG. 2. (Color online) Dependence of the emission energy of QDs on the indented position of the nanoprobe (F=1.3 mN). (a) The whole experimental results. (b) Illustration of the typical emission traces from QDs [part of the total 42 traced streaks, refer to the abscissa for the relative position in (a)].

TABLE I. Material parameters used in the calculation of strain and energy-band shift. The values of InAs are only used for the linear interpolation of $In_{0.5}Ga_{0.5}As$.

	GaAs	$In_{0.5}Ga_{0.5}As$	InAs
a (Å)	5.6533	5.8558	6.0584
c_{11} (GPa)	118.8	101.05	83.29
c_{12} (GPa)	53.8	49.53	45.26
c_{44} (GPa)	59.4	49.49	39.59
a_c (eV)	−7.63	−6.06	−4.49
a_v (eV)	−1.00	−0.93	−0.85
b (eV)	−1.77	−1.81	−1.85
d (eV)	−3.10	−3.21	−3.32
Δ_0 (eV)	0.33	0.35	0.36

approaching nanoprobe rather than behind it, as will be discussed in Sec. IV. This is because the excited laser illuminates the area in front of the approaching nanoprobe. No permanent damage was resulted in QDs or the nanoprobe during experiment since the PL results were repeated when the nanoprobe was rescanned along the same trace.

III. STRAIN ANALYSIS

The FE method is used to develop a 3D model to calculate the strain field in and around a specific QD that is produced by the lattice mismatch and the indentation force. In the model, elastic anisotropy is adopted, with elastic constants of GaAs and $In_{0.5}Ga_{0.5}As$ listed in Table I.[29] For the nanoprobe, Young's modulus and Poisson's ratio of SiO_2 are taken to be $E=73.1$ GPa and $\nu=0.17$, respectively.[30] Here, we assume that the chemical composition of the QDs is uniform ($In_{0.5}Ga_{0.5}As$) and the QD shape is (110) faceted pyramidal in the typical and ideal case, although the composition and shape of the QDs fluctuate due to the growth conditions (growth temperature, growth rate, and capping process).[31–34]

Based on the microscopic observations,[35] a QD with a base width ($2l$) of 20 nm and a height (h) of 7 nm is modeled. The GaAs capping layer in our sample has a thickness (t) of 50 nm, and the nanoprobe has a diameter ($2R$) of 850 nm, as shown in Fig. 3. Due to the large difference in size between the QD and the nanoprobe apex, the submodeling technique is employed in the strain analysis about the

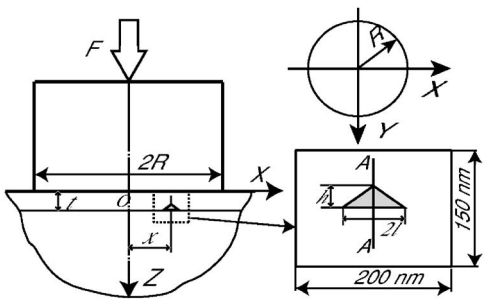

FIG. 3. Illustration of the simulation model in the nanoprobe indentation (not to scale).

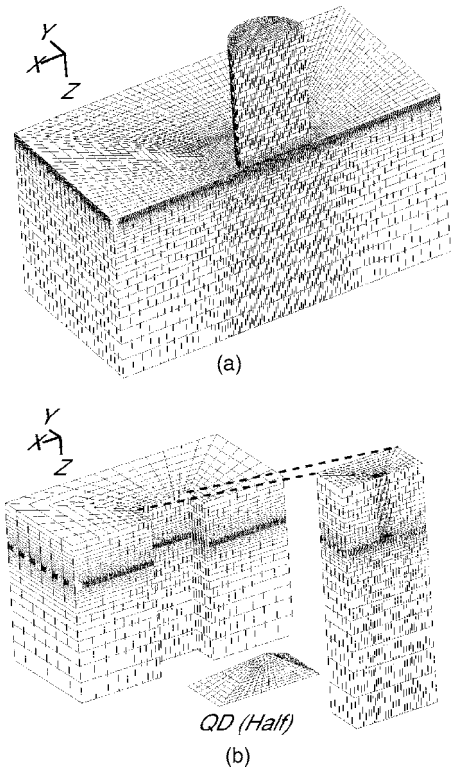

FIG. 4. The FE model. (a) The mesh of the global model; (b) Submodel along x axis (left side), half of the QD is modeled due to the symmetry. The small FE model (right side) which is the center part of the large submodel is used for lattice-mismatched strain calculation. The mesh of the QD is also shown in the insert.

nanoprobe indentation. In the global indentation model, we neglect the QDs and the sample is assumed to be homogeneous GaAs since the size of the QD is 100 times smaller than the dimensions of the sample in the global model ($4000\times4000\times2000$ nm^3 in x, y, and z directions). With the coordinates shown in Fig. 3, the submodel used to simulate the indentation-induced deformation in and around a specific QD has the dimensions of 200 nm in the x and y directions, and 150 nm in the z direction. Both the global model and submodel are taken large enough to suppress the influences of the surrounding boundary. Using this submodeling technique, the indentation-induced strain in and around the QD is calculated.

In the calculation of the lattice-mismatch strain, the dimension of the unit cell in the x and y directions is 50 nm with the coordinates shown in Fig. 3, determined from the average space between the neighboring QDs [the density of the QDs is $(5-6)\times10^{10}$ cm^{-2}]. The periodic boundary condition is adopted in the x and y directions and $u_z=0$ at the bottom surface ($z=150$ nm) for the calculation of lattice-mismatch-induced strain. Figure 4(a) shows the mesh division of the global model. Half of the nanoprobe indenter and the sample of GaAs are modeled due to the symmetric x-z plane. Figure 4(b) shows the mesh of the half submodel to calculate the indentation-induced strain and the mesh of the half FE model to calculate the mismatch-induced strain. As shown in Fig. 4(b), the FE model to calculate the mismatch-induced strain is only a part of the submodel to calculate the

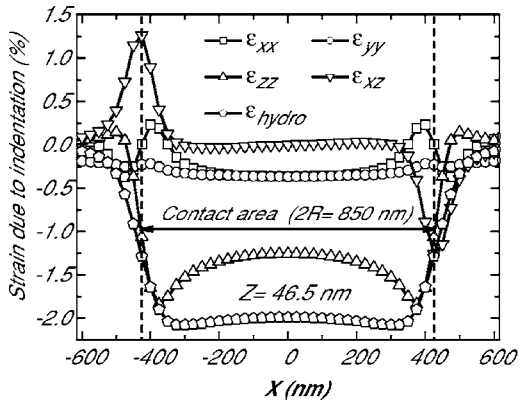

FIG. 5. Strain components along the x axis due to indentation (1.3 mN) calculated in the global model (GaAs matrix) at z =46.5 nm in the x-z plane.

indentation-induced strain, and the mesh division is identical in their common part. When the calculated QD is not located in the symmetric x-z plane, a full submodel is required.

With the above-mentioned global model, the indentation effects between the nanoprobe flat apex and the top surface of the QD sample are calculated using a small sliding contact with the assumption of no friction. The indentation force is 1.3 mN measured by the load cell. Our calculations with friction coefficients of μ=0.1 and μ=0.2 show that the friction effects are negligible in the current work. With the displacement calculated in the global model, we obtain the indentation-induced strain field in and around the QD at any position under the contact area using the submodeling technique. The lattice-mismatched strain between the $In_{0.5}Ga_{0.5}As$ QD and the GaAs matrix is calculated in the FE model of lattice mismatch according to Mura's theory on eigenstrain.[36] The lattice-mismatched QDs within the matrix can be assumed to be one type of inclusion for a given eigenstrain, and the total strain e_{ij} is given by the sum of the eigenstrain ε_{ij}^* and the elastic strain ε_{ij},

$$e_{ij} = \varepsilon_{ij} + \varepsilon_{ij}^*, \tag{1}$$

where i and j take x, y, or z. The eigenstrain due to the lattice mismatch, $\varepsilon_{ij}^*=\varepsilon^*\delta_{ij}$, can be calculated as

$$\varepsilon^* = \frac{a_{In_{0.5}Ga_{0.5}As} - a_{GaAs}}{a_{GaAs}} = 0.0358, \tag{2}$$

where δ_{ij}=1 when i=j, and δ_{ij}=0 when $i \neq j$. a_{GaAs} and $a_{In_{0.5}Ga_{0.5}As}$ are the lattice constants of GaAs and $In_{0.5}Ga_{0.5}As$, respectively. In the FE calculation, the thermal expansion coefficients of the QD and the matrix are set as ε^* and 0, respectively, and the temperature of the FE model is raised by 1 K. Finally, the strain field in and around the QD, which is produced by the combination of the indentation force and the lattice mismatch, is obtained by the summation of the indentation-induced strain and lattice-mismatch-induced strain.

Figure 5 shows the elastic normal and shear strain components along the x axis in the global model in the x-z plane and z=46.5 nm, which corresponds to the center level of the QD layer. It can be seen that ε_{yy} and ε_{zz} have compressive strain within the entire contact region, while ε_{xx} is tensile in the region close to the contact edge ($\bar{r} \equiv |x|/R > 0.82$). Among the three normal strains (ε_{xx}, ε_{yy}, and ε_{zz}), ε_{zz} is outstanding with its magnitude, about five times that of ε_{xx} and ε_{yy} in the center part of the contact region ($\bar{r} < 0.6$). The hydrostatic strain (ε_{hydro}) has weak dependence on the x value and decreases quickly with position approaching the contact edge ($\bar{r} > 0.7$). As we discussed in another paper,[26] the hydrostatic strain dominates the energy shift of the InGaAs/GaAs system since the shift of the conduction band is far larger than the valence band. It is noteworthy that ε_{xz} has a δ-shaped peak about ±0.013 at the edge of the contact area. In Fig. 6, the distribution of ε_{xz} in the GaAs matrix due to the indentation is plotted. The indentation results in a maximum area of $|\varepsilon_{xz}|$ in the GaAs matrix under the edge of the contact region. As discussed in Sec. V, the maximum area of $|\varepsilon_{xz}|$ causes a minimum-energy valley for the holes in the GaAs matrix. The strain distribution in and around the QD due to the indentation and lattice mismatch calculated in the submodel has already been discussed in detail in our previous work,[26] where we found that the strain due to lattice mismatch was strongly localized in the QD region and disappeared quickly to zero in the matrix (about 10 nm outside the QD). The distribution of the superposed strain can be described by the mismatch-induced strain modulated by the indentation-induced strain.

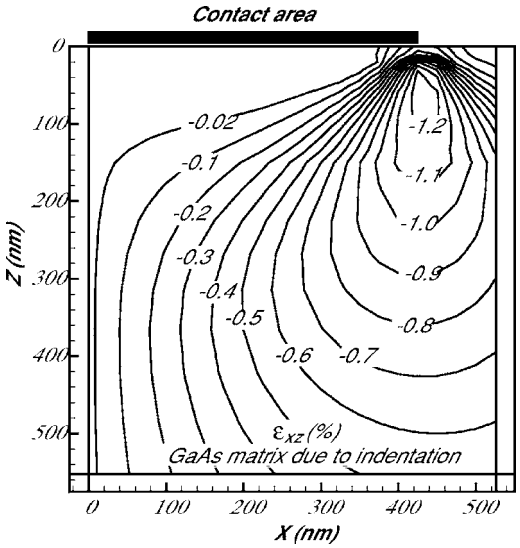

FIG. 6. The distribution of ε_{xz} in the GaAs matrix due to indentation (1.3 mN).

IV. IDENTIFICATION OF THE QD LOCATION

Based on the strain field obtained from the FE analysis, the strain-induced shifts of the discrete energy levels of the QD are calculated using Pikus-Bir theory.[37] In this theory, the elastic strain field is coupled to the quantum-mechanical behavior of the charged carriers in semiconductors through the deformation potentials of the materials. In general, band gaps of GaAs and InGaAs are enlarged by the hydrostatic

pressure, leading to a blueshift of PL peak. In our indentation experiment, the compressive hydrostatic strain component is predominant over the shear strain, which results in blueshift of the PL from QDs. Shear strain components contribute only a small amount through the shift of the valence band. For the valence-band shifts of both InGaAs QD and GaAs matrix, the six-band strain-dependent Hamiltonian is written as

$$H_{\varepsilon}^{V} = -\begin{bmatrix} P+Q & -S & R & 0 & \sqrt{\frac{1}{2}}S & -\sqrt{2}R \\ -S^{\dagger} & P-Q & 0 & R & \sqrt{2}Q & -\sqrt{\frac{3}{2}}S \\ R^{\dagger} & 0 & P-Q & S & -\sqrt{\frac{3}{2}}S^{\dagger} & -\sqrt{2}Q \\ 0 & R^{\dagger} & S^{\dagger} & P+Q & \sqrt{2}R^{\dagger} & \sqrt{\frac{1}{2}}S^{\dagger} \\ \sqrt{\frac{1}{2}}S^{\dagger} & \sqrt{2}Q & -\sqrt{\frac{3}{2}}S & \sqrt{2}R & P+\Delta_0 & 0 \\ -\sqrt{2}R^{\dagger} & -\sqrt{\frac{3}{2}}S^{\dagger} & -\sqrt{2}Q & \sqrt{\frac{1}{2}}S & 0 & P+\Delta_0 \end{bmatrix} \begin{matrix} \left|\frac{3}{2},\frac{3}{2}\right\rangle \\ \left|\frac{3}{2},\frac{1}{2}\right\rangle \\ \left|\frac{3}{2},-\frac{1}{2}\right\rangle \\ \left|\frac{3}{2},-\frac{3}{2}\right\rangle \\ \left|\frac{1}{2},\frac{1}{2}\right\rangle \\ \left|\frac{1}{2},-\frac{1}{2}\right\rangle \end{matrix},$$

$$P = a_v(\varepsilon_{xx}+\varepsilon_{yy}+\varepsilon_{zz}), \quad Q = b\left[\varepsilon_{zz}-\frac{1}{2}(\varepsilon_{xx}+\varepsilon_{yy})\right],$$

$$R = \frac{\sqrt{3}}{2}b(\varepsilon_{xx}-\varepsilon_{yy}) - id\varepsilon_{xy}, \quad S = -d(\varepsilon_{xz}-i\varepsilon_{yz}), \tag{3}$$

where a_v, b, and d are the hydrostatic and two shear deformation potentials, respectively, and Δ_0 is the split-off energy gap.[38] The matrix elements indicated with a superscript of † are the corresponding conjugate complexes. In the $In_{0.5}Ga_{0.5}As/GaAs$ QD system, we calculated the energy shift in the six-band Hamiltonian neglecting the interaction between the conduction band and valence band because the conduction band and valence band of strain-free bulk $In_{0.5}Ga_{0.5}As$ are separated by a rather large energy gap of 850 meV and the strain due to indentation and lattice mismatch is not as large as the large-misfit material pair such as the InAs/GaAs QD system.[39] The shifts of the valence bands, ΔE_v, are calculated as eigenvalues of H_{ε}^{V},

$$|H_{\varepsilon}^{V} - \Delta E_v I| = 0, \tag{4}$$

where I is an identity matrix and $|\,|$ denotes the determinant. For the conduction band of III-V semiconductors, the effect of strain is to produce a hydrostatic energy shift proportional to the fractional volume change given by

$$\Delta E_c = a_c(\varepsilon_{xx}+\varepsilon_{yy}+\varepsilon_{zz}), \tag{5}$$

where a_c is the deformation potential of the conduction band.[38] Our previous calculations showed that the indentation-induced energy shifts of the QDs were mainly determined by the strain-induced potential change, not by the strain-induced change in the confinement barriers (<2 meV).[26] Thus, we can approximate that the energy shifts of the QD levels in our experiments are the same as the difference of the shifts between the conduction-band minimum (CBM) and the valence-band maximum (VBM) of the QD (neglecting the quantum confinement effects). For the strain components at position (x,y,z), the energy-band-gap shift is

$$\Delta E(x,y,z) = \Delta E_c(x,y,z) - \Delta E_v(x,y,z). \tag{6}$$

The energy-band-gap shift (ΔE) of a QD under the indentation force (F) can be calculated with the volume average assumption,

$$\Delta E = \frac{1}{V_0}\int_{V_0} \Delta E(x,y,z)dV, \tag{7}$$

where the volume integration is performed over the QD volume. This spatial averaging in our calculation is the same scheme adopted by Pryor *et al.*, where they obtained reasonable results for the band-edge diagrams for strained III-V semiconductor quantum wells, wires, and dots.[40] The deformation potentials used in the calculation were listed in Table I,[41] in which the parameters of $In_{0.5}Ga_{0.5}As$ were obtained by linear interpolation between those of GaAs and InAs.[41]

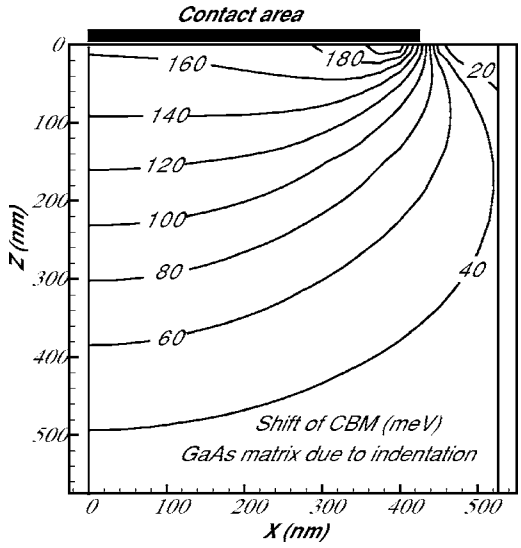

FIG. 7. Shift of CBM in the GaAs matrix due to indentation (1.3 mN).

In Figs. 7 and 8, the energy shifts of CBM and VBM of the GaAs matrix due to indentation are plotted, respectively. It can be seen that the CBM and VBM of the matrix under the nanoprobe shift significantly. The shift decreased quickly away from the indented region. At the depth where the QD layer exists ($z=50$ nm), the upward shift of CBM due to the large hydrostatic pressure is predominant compared with the shift of VBM under the contact region ($x<425$ nm), leading to a wider gap between the CBM and VBM. Since the lattice-mismatch-induced hydrostatic strain component is also compressive in an InGaAs/GaAs quantum dots, an additional blueshift of PL from QDs is expected when the hydrostatic strain due to indentation superposed on the one due to lattice mismatch. In Fig. 8, it can be seen that the indentation results in a maximum shift of VBM around the boundary of the contact area. This is also shown clearly in Fig. 9,

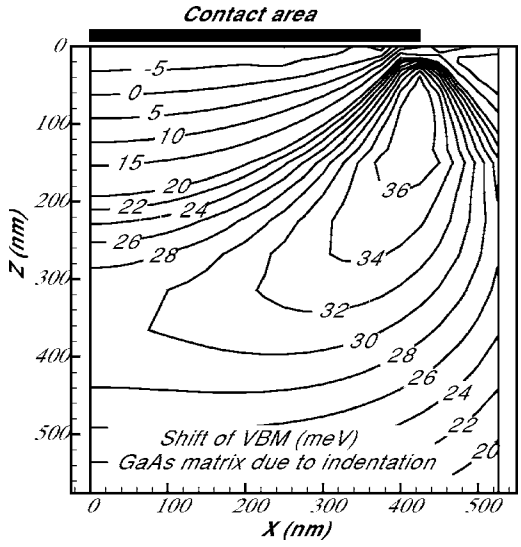

FIG. 8. Shift of VBM in the GaAs matrix due to indentation (1.3 mN).

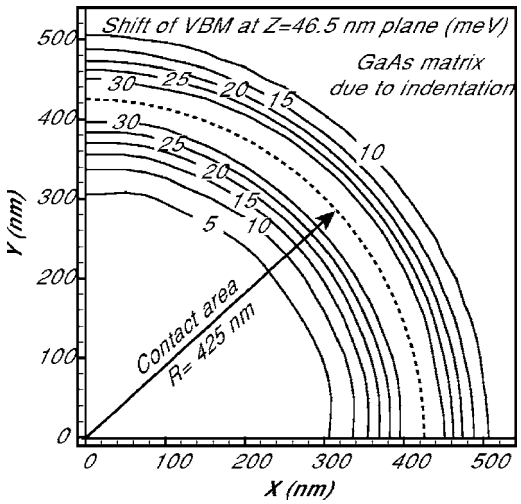

FIG. 9. Shift of VBM in the GaAs matrix due to indentation (1.3 mN). The slice is plotted at $z=46.5$ nm plane and the dashed line in the figure is the boundary of the contact area.

which plots the shift of VBM in the x-y plane at $z=46.5$ nm. In addition, we can find in Fig. 9 that the indentation-induced energy shift of VBM in the GaAs matrix is almost axisymmetric about the rotation axis of the cylindrical nanoprobe. Our calculation shows that the energy shift of CBM in the GaAs matrix by the indentation is also almost axisymmetric about the rotation axis of the cylindrical nanoprobe.

Figure 10 shows the indentation-induced energy shift of QD levels, calculated by the difference of the energy shift of QD levels in lattice-mismatch state and superposition state (lattice mismatch and indentation). We cannot directly use the energy shift of QD levels by the indentation without taking into account the influence of lattice-mismatch strain because the calculation with (without) the lattice-mismatch strain leads the heavy hole band (light hole band) to be the top valence band in the QD.[42] In Fig. 10, every corner

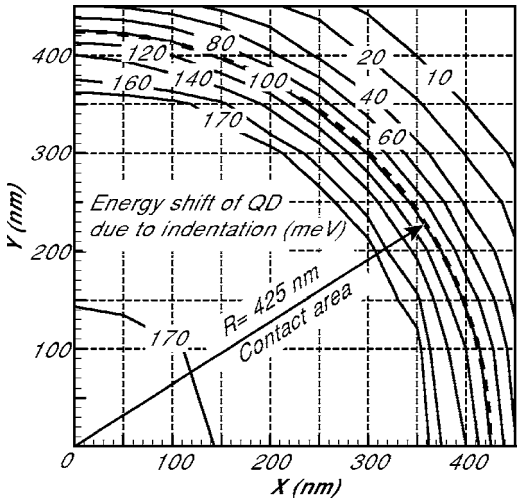

FIG. 10. Indentation induced energy shift of individual QDs calculated in submodel ($F=1.3$ mN). The cross points of the dashed grid represent the individual InGaAs QDs.

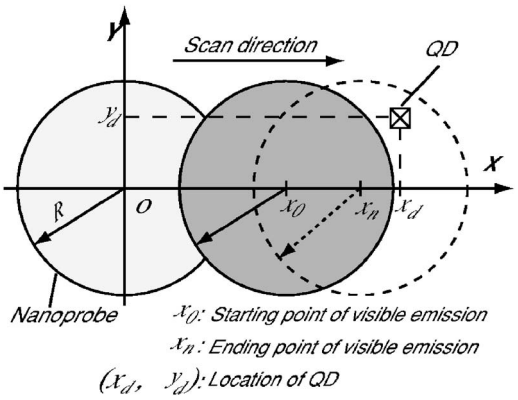

FIG. 11. Illustration of the coordinate used in the location identification of QD.

"node" of the "grid" represents a QD, and the contours are plotted based on the energy shifts of these individual QDs. The energy shift of QDs shows a large gradient around the boundary of the nanoprobe contact area. The annular region with large gradient in ΔE in Fig. 10 coincides with the annular region with maximum shift in VBM in Fig. 9. It is also seen that ΔE under the contact region is almost axisymmetric about the rotation axis of the cylindrical nanoprobe, resembling the CBM and VBM shift of the GaAs matrix in the distribution. Since the indentation-induced energy shift of QDs has a strong dependence on the location of each QD relative to the nanoprobe as shown in Fig. 10, we can estimate the position of QDs by their emission traces.

Assuming the initial location of the nanoprobe is the origin of Fig. 11. During the experiment, the nanoprobe moves on the fixed QD sample along the x axis with indentation. During the horizontal scan of the nanoprobe, PL from a QD (x_d, y_d) is first detected as a trace when the location of the nanoprobe is x_0. It finally disappears when the location of the nanoprobe is x_n. In order to evaluate the location of the QD (x_d, y_d) its emission trace is traced from Fig. 2 as illustrated in Fig. 12, in which the experimental energy change compared with the starting point is defined as

$$\delta E^{\exp}(x_k) = E(x_k) - E(x_0), \tag{8}$$

where $E(x_0)$ and $E(x_k)$ are the emission energies of the first point and the kth point of the emission trace, respectively. We introduce another variant ΔE_0 defined as

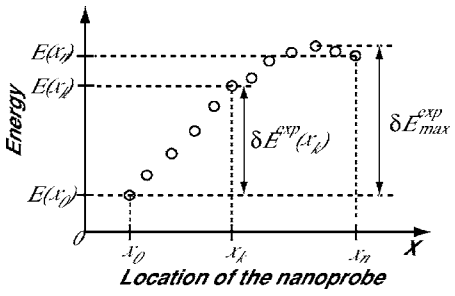

FIG. 12. Illustration and definition of the emission traces obtained in scan experiment.

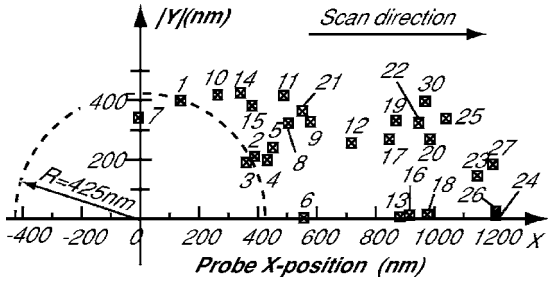

FIG. 13. The identified locations of typical QDs by the horizontal scan experiment (part of the total 42 QDs). The QDs are represented by the rectangular symbols and the serial numbers correspond to the traced peak in Fig. 2.

$$\Delta E_0 = E(x_0) - E_g, \tag{9}$$

where E_g is the initial emission energy of the QD in the load-free state and ΔE_0 is the indentation-induced energy shift of the QD when the nanoprobe is indented at x_0.

In Fig. 2, the emission traces varied in shapes and were at different indented locations along the horizontal scan axis. Since the indentation force was constant in the experiment (1.3 mN), we can reasonably attribute the different locations and shapes of the emission traces to the QD locations relative to the nanoprobe. The segment of emission traces, which is in best agreement between experiment and simulation can be found by comparing the shape of the emission traces in Fig. 2 to any part of the predicted emission traces parallel to the x axis at any y values (along with the horizontal scan of the nanoprobe). Based on the least-squares method, this idea can be written as follows:

$$\text{Position: } J = (\delta E^{\exp}_{\max})^{-2} \sum_{k=0}^{n} \{\delta E^{\exp}(x_i) + \Delta E_0^* - \Delta E^{sim}(x_k; x_d^*, y_d^*)\}^2, \quad \min J, \tag{10}$$

where ΔE_0^*, x_d^*, and y_d^* are the variants for ΔE_0, x_d, and y_d, respectively. ΔE_0, x_d, and y_d take the values of ΔE_0^*, x_d^*, and y_d^* when the minimum of J is found for the emission trace. $\delta E^{\exp}_{\max}$ is used for the nondimensional. With Eq. (10), the locations of typical QDs corresponding to the emission traces are identified as shown in Fig. 13, in which each of the identified QDs is plotted at the location of the QD by a rectangular symbol. The coordinate in the y direction is the absolute value due to the symmetry (the indenter is cylindrical and it scans along the x axis in the experiment). The sign of the y value will be determined by y-scan experiments. Our calculations with another set of elastic constants and deformation potentials[39] showed that the identified locations of QD09 and QD15 in Fig. 13 changed from (579,|327|) and (380,|382|) to (564,|334|) and (392,|385|), respectively. The small changes (less than the dimension of the QD) reveal that our simulation results are robust under the variation of material parameters. A representative comparison between the experimental and the simulated results is plotted in Fig. 14. The abscissa is the difference in the x coordinate between the nanoprobe and the QD. The ordinate is the energy shifts of $\Delta E^{\exp} + \Delta E_0$ (shown in open circle) and ΔE^{sim} (shown in

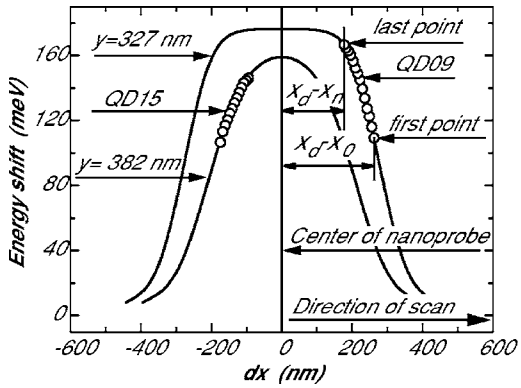

FIG. 14. Comparison between the experiment and simulation results for some emission traces. The abscissa is the difference in the x coordinate between the nanoprobe and the QD. The ordinate is the energy shifts of $\Delta E^{\exp}+\Delta E_0$ (shown in open circles) and ΔE^{sim} (shown in solid lines).

solid line). For example, the QD09 emission trace corresponds to the No.9 peak in Fig. 2, and the location of No.9 QD is 327 nm away from the scan axis in Fig. 14 ($|y_d|$ =327 nm). Its emission was observed from the point where the center of the nanoprobe is 262 nm behind the QD along the horizontal scan direction ($x_d-x_0=262$ nm) to the point where the center of the nanoprobe is 176 nm behind the QD along the horizontal scan direction ($x_d-x_n=176$ nm). In addition, see Fig. 11 for an illustration. Figure 14 shows that the results of the experiment are in good agreement with those of the simulation. Different shapes of emission traces correspond to the different locations of QDs. The positive (negative) gradient of the slope of the emission trace in Fig. 2 corresponds to the fact that the center of the nanoprobe is behind (in front of) the QD along the horizontal scan direction. In Fig. 15, the relative positions between the center of the nanoprobe and the 42 emission traces are plotted. It is remarkable that all the observed emission traces are located around the edge of the contact area ($R=425$ nm), within an annular region with radius 314 nm$<r<$478 nm, especially in the vicinity of $\bar{r}=r/R=1.0$.

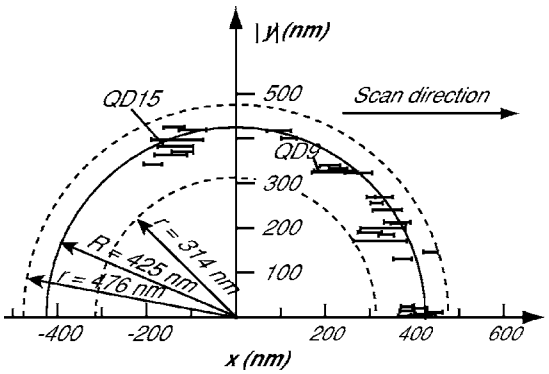

FIG. 15. Illustration of the relative locations of emission traces in experiment (Fig. 2) to the indented location. Each emission trace starts from right and ends at left side in this figure. Emission traces from QD9 and QD15 corresponds to the emission lines in Fig. 14.

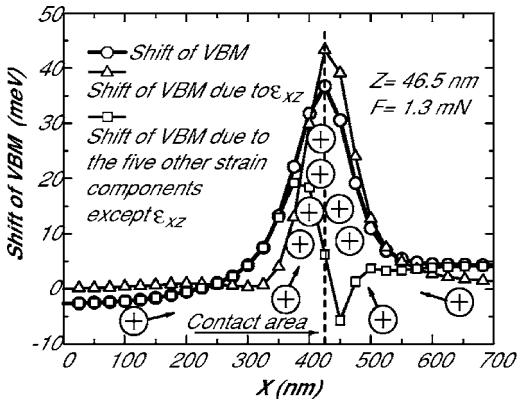

FIG. 16. Illustration of the holes concentration due to nanoprobe indentation in global model. The shifts of VBM are plotted according to the results of GaAs matrix at $z=46.5$ nm in the x-z plane.

V. DISCUSSION

The reason why only the emissions of the QDs located in the annular region around the contact edge were observable in our experiment can be found in a comparison of Fig. 9 with Fig. 15. The annular region with a large upward shift of VBM in Fig. 9 coincides with the annular region where the observable QDs are located. This coincidence suggests that the large upward shift of VBM around the contact edge is critical for the emissions from the QDs shown in Fig. 15. Recall from Figs. 6 and 8 that the similar distribution of ε_{xz} and shift of VBM around the contact edge is a hint of the possible dependence of a large upward shift of VBM on the δ-shaped maximum of $|\varepsilon_{xz}|$ around the contact edge. Figure 5 shows that the indentation results in a peak of about 0.013 for the $|\varepsilon_{xz}|$ at $\bar{r}=1.0$. When only ε_{xz} is the nonzero strain component, the dependence of VBM shift on ε_{xz} can be calculated as follows:[26]

$$\Delta E_v(\varepsilon_{xz}) = [-\xi^3 + \sqrt{\xi^6 - (\xi^2 + (d\varepsilon_{xz})^2)^3}]^{1/3} + [-\xi^3 - \sqrt{\xi^6 - (\xi^2 + (d\varepsilon_{xz})^2)^3}]^{1/3} - \xi, \quad (11)$$

where $\xi=\Delta_0/3$ and d is the shear deformation potential. Using Eq. (11), we can estimate that the peak of $|\varepsilon_{xz}|$ around the contact edge causes the upward shift of VBM for about 40 meV, which is coincident with the maximum value in Figs. 8 and 9. To determine the relationship between the large upward shift of VBM and the peak of $|\varepsilon_{xz}|$ around the contact edge, we plot the VBM shift of the GaAs matrix in the global model at $z=46.5$ nm and $y=0$ nm under the indentation force of 1.3 mN in Fig. 16. The shift of VBM in Fig. 16 has a maximum value under the edge of the contact area. Compared with the five other strain components (ε_{xx},ε_{yy},ε_{zz}, ε_{xy}, and ε_{yz}), $|\varepsilon_{xz}|$ has a predominant contribution to the large upward shift of VBM around the contact edge. Since $|\varepsilon_{xz}|$ is localized around the contact edge, the upward shift of VBM induced by $|\varepsilon_{xz}|$ is large only around the contact edge. The holes in the GaAs matrix tend to move into this narrow energy valley, resulting in a high hole density in the annular region around the contact edge. The high density of holes enhances the PL of the QDs in this region probably with the similar mechanism as p-type doping.[43] Consequently, only

the PL of the QDs located at this edge can be observed effectively. According to a simulation work with atomistic empirical pseudopotential,[44] a truncated cone-shaped $In_{0.5}Ga_{0.5}As/GaAs$ QD (height of 3.5 nm, base diameter of 20 nm, and top diameter of 16 nm) has a ground emission energy of 1282 meV, together with the confinement potential of 107±1 meV for electrons. With our measured PL peak energy without indentation (1270 meV) and the size of our pyramidal $In_{0.5}Ga_{0.5}As/GaAs$ QDs (base of 20 nm, height of 7 nm), we reasonably assume that the confinement potential for electrons in our QD is 110±20 meV, taking into account of the shape and size effects.[45] The largest repulsive potential slope in Fig. 7 is 28 meV within the length of a QD base (20 nm) along the x direction at $z=50$ nm. Thus, the electrons are confined strong enough against the repulsive slope generated by the indentation. The enhanced PL of QDs is obviously helpful in the observation of the optical properties of QDs. However, this phenomenon depends on the radius (R) of the nanoprobe and the indentation force (F). When the nominal indentation pressure $[P_N=F/(\pi R^2)]$ is constant, the hole energy valley tends to locate in the region close to the top free surface with a decrease in R (Fig. 17). The larger the radius of the nanoprobe, the wider the energy valley of the hole. Consequently, in the indentation experiment, it is easier to observe the enhancement of the PL of QDs with a larger nanoprobe. For the indentation experiment with a small nanoprobe (<100 nm), one should adjust the indentation force and thickness of the capping layer to obtain the enhanced PL of QDs.

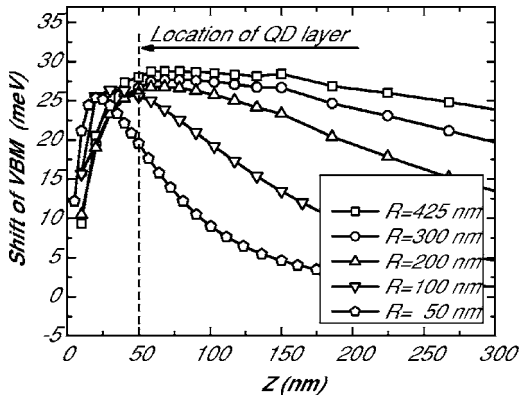

FIG. 17. Comparison of the indentation-induced energy shift of VBM in GaAs matrix with nanoprobes different in radius. The shifts of VBM are plotted according to the results of GaAS matrix along the z axis under the contact edge (at top free surface, $z=0$ nm). The nominal indentation pressure is equivalent to the uniform pressure of 1.0 mN force on a nanoprobe with a radius of 425 nm.

VI. CONCLUSION

In conclusion, we have succeeded in the simultaneous measurement of the indentation force and PL of QDs in the nanoprobe indentation experiment with a horizontal scan, which enables us to evaluate the location of QDs. The location of QDs relative to the nanoprobe was successfully evaluated by comparison of the emission traces from QDs obtained in the horizontal scanning experiments and simulation. In this experiment, we effectively observed only the emission traces of QDs located at the edge of the contact area. The simulation revealed that the increase in the strain component $|\varepsilon_{xz}|$ at the edge of the nanoprobe was responsible for the large upward shift of the VBM (about 40 meV), which resulted in an annular energy minimum valley for the holes in the GaAs matrix. Consequently, the holes were concentrated in this annular region and enhanced the PL of QDs located in this region. The strain-induced hole concentration realized in our nanoprobe indentation provides an effective way to evaluate the influence of p-type doping on the electronic and optical properties of QDs, since the effects of the hole concentration can be tuned by the indentation force unlike in real p-type doping experiments.

ACKNOWLEDGMENTS

This research was partially supported by the Ministry of Education, Science, Sports and Culture of the Japanese Government, Grant-in-Aid for Scientific Research (C), No. 18560069, 2006–2007. One of the authors (Y.H.L.) gratefully acknowledges support from the Ministry of Education, Science, Sports and Culture of the Japanese Government.

*Corresponding author. FAX: +81-48-856-2577, Electronic address: yarai@mech.saitama-u.ac.jp

[1] D. Bimberg, M. Grundmann, and N. N. Ledentsov, *Quantum Dot Heterostructures* (Wiley, New York, 1999).
[2] D. Bimberg, J. Phys. D **38**, 2055 (2005).
[3] A. Strittmatter, T. D. Germann, Th. Kettler, K. Posilovic, U. W. Pohl, and D. Bimberg, Appl. Phys. Lett. **88**, 262104 (2006).
[4] M. T. Todaro, M. De Giorgi, V. Tasco, M. De Vittorio, R. Cingolani, and A. Passaseo, Appl. Phys. Lett. **84**, 2482 (2004); V. Tasco, M. T. Todaro, M. De Vittorio, M. De Giorgi, R. Cingolani, A. Passaseo, J. Ratajczak, and J. W. Katcki, *ibid.* **84**, 4155 (2004).
[5] I. L. Krestnikov, N. A. Maleev, A. V. Sakharov, A. R. Kovsh, A. E. Zhukov, A. F. Tsatsul'nikov, V. M. Ustinov, Zh. I. Alferov, N. N. Ledentsov, D. Bimberg, and J. A. Lott, Semicond. Sci. Technol. **16**, 844 (2001); A. Monakhov, A. Krier, and V. V. Sherstnev, *ibid.* **19**, 480 (2004).
[6] C. E. Pryor and M. E. Flatte, Phys. Rev. Lett. **91**, 257901 (2003).
[7] K. D. Osbron, Mark W. Keller, and R. P. Mirin, Physica E (Amsterdam) **21**, 501 (2004).
[8] S. H. Hwang, J. C. Shin, J. D. Song, W. J. Choi, J. I. Lee, H. Han, and S.-W. Lee, Microelectron. Eng. **78-79**, 229 (2005).
[9] L. Fu, H. H. Tan, I. McKerracher, J. Wong-Leung, C. Jagadish, N. Vukmirovic, and P. Harrison, J. Appl. Phys. **99**, 114517 (2006).

[10] M. T. Todaro, V. Tasco, M. De Giorgi, M. De Vittorio, R. Cingolani, A. Passaseo, F. Romanato, and E. Di Fabrizio, Microelectron. Eng. **73-74**, 757 (2004).
[11] M. E. Ikpi, P. Atkinson, S. P. Bremner, and D. A. Ritchie, J. Cryst. Growth **278**, 113 (2005).
[12] S.-D. Chen, Ch-Y. Tsai, and S.-Ch Lee, J. Nanopart. Res. **6**, 407 (2004).
[13] Y. Temko, T. Suzuki, P. Kratzer, and K. Jacobi, Phys. Rev. B **68**, 165310 (2003); Y. Temko, T. Suzuki, M. C. Xu, K. Potschke, D. Bimberg, and K. Jacobi, *ibid.* **71**, 045336 (2005).
[14] M. C. Xu, Y. Temko, T. Suzuki, and K. Jacobi, Surf. Sci. **576**, 89 (2005).
[15] M. Sztucki, T. U. Schulli, T. H. Metzger, E. Beham, D. Schuh, and V. Chamard, Superlattices Microstruct. **36**, 11 (2004).
[16] A. I. Tartakovskii, M. N. Makhonin, I. R. Sellers, J. Cahill, A. D. Andreev, D. M. Whittaker, J.-P. R. Wells, A. M. Fox, D. J. Mowbray, M. S. Skolnick, K. M. Groom, M. J. Steer, H. Y. Liu, and M. Hopkinson, Phys. Rev. B **70**, 193303 (2004).
[17] F. Guffarth, R. Heitz, A. Schliwa, O. Stier, N. N. Ledentsov, A. R. Kovsh, V. M. Ustinov, and D. Bimberg, Phys. Rev. B **64**, 085305 (2001).
[18] I. E. Itskevich, S. G. Lyapin, I. A. Troyan, P. C. Klipstein, L. Eaves, P. C. Main, and M. Henini, Phys. Rev. B **58**, R4250 (1998).
[19] H. D. Robinson, M. G. Muller, B. B. Goldberg, and J. L. Merz, Appl. Phys. Lett. **72**, 2081 (1998).
[20] A. Chavez-Pirson, J. Temmyo, and H. Ando, Physica E (Amsterdam) **7**, 367 (2000).
[21] H. T. Johnson, R. Bose, B. B. Goldberg, and H. D. Robinson, Int. J. Multiscale Comp. Eng. **1**, 33 (2003).
[22] H. T. Johnson and R. Bose,J. Mech. Phys. Solids **51**, 2085 (2003).
[23] K. Ozasa, Y. Aoyagi, A. Yamane, and Y. Arai, Appl. Phys. Lett. **83**, 2247 (2003).
[24] K. Ozasa, Y. Aoyagi, M. Hara, M. Maeda, A. Yamane, and Y. Arai, Physica E (Amsterdam) **21**, 265 (2004).
[25] A. M. Mintairov, K. Sun, J. L. Merz, C. Li, A. S. Vlasov, D. A. Vinokurov, O. V. Kovalenkov, V. Tokranov, and S. Oktyabrsky, Phys. Rev. B **69**, 155306 (2004).
[26] Y.-H. Liang, Y. Arai, K. Ozasa, M. Ohashi, and E. Tsuchida, Physica E (Amsterdam) **36**, 1 (2007).
[27] K. Ozasa, Y. Aoyagi, Y. J. Park, and L. Samuelson, Appl. Phys. Lett. **71**, 797 (1997).
[28] K. Ozasa and Y. Aoyagi, J. Cryst. Growth **188**, 370 (1998).
[29] S. Adachi, J. Appl. Phys. **53**, 8775 (1982).
[30] E. H. Bogardus, J. Appl. Phys. **36**, 2504 (1965).
[31] D. M. Bruls, J. W. A. M. Vugs, P. M. Koenraad, H. W. M. Salemink, J. H. Wolter, M. Hopkinson, M. S. Skolnick, F. Long, and S. P. A. Gill, Appl. Phys. Lett. **81**, 1708 (2002).
[32] C.-H. Hsu, H.-Y. Lee, Y.-W. Hsieh, Y. P. Stetsko, M.-T. Tang, K. S. Liang, N. T. Yeh, J.-I. Chyi, and D. Y. Noh, Physica B **336**, 98 (2003).
[33] A. Lemaitre, G. Patriarche, and F. Glas, Appl. Phys. Lett. **85**, 3717 (2004).
[34] V. G. Dubrovskii, G. E. Cirlin, Yu. G. Musikhin, Yu. B. Samsonenko, A. A. Tonkikh, N. K. Polyakov, V. A. Egorov, A. F. Tsatsul'nikov, N. A. Krizhanovskaya, V. M. Ustinov, and P. Werner, J. Cryst. Growth **267**, 47 (2004).
[35] K. Ozasa, Y. Aoyagi, M. Iwaki, and H. Kurata, J. Appl. Phys. **94**, 313 (2003).
[36] T. Mura, *Micromechanics of Defects in Solids*, 2nd ed. (Martinus Nijhoff, Boston, 1987).
[37] G. L. Bir and G. E. Pikus, *Symmetry and Strain-Induced Effects in Semiconductors* (Wiley, New York, 1974).
[38] J. Singh, *Physics of Semiconductors and Their Heterostructures* (McGraw-Hill, New York, 1993).
[39] I. Vurgaftman, J. R. Meyer, and L. R. Ram-Mohan, J. Appl. Phys. **89**, 5815 (2001).
[40] C. E. Pryor and M.-E. Pistol, Phys. Rev. B **72**, 205311 (2005).
[41] L. W. Wang, A. J. Williamson, A. Zunger, H. Jiang, and J. Singh, Appl. Phys. Lett. **76**, 339 (2000).
[42] Y.-H. Liang, Y. Arai, M. Ohashi, K. Ozasa, M. Hara, and M. Maeda, Proceedings of the Sixth International Conference on Intelligent Materials and Systems—Nanotechnology Frontier, Tokyo, Japan, 2005 (unpublished), p. 311.
[43] N. Kumagai, K. Watanabe, S. Tsukamoto, and Y. Arakawa, *2005 International Conference on Indium Phosphate and Related Materials Glasgow, Scotland, UK, 2005* (IEEE, Piscataway, NJ, 2005), IEEE Catalog No. 05CH37633, p. 53.
[44] J. Shumway, A. J. Williamson, A. Zunger, A. Passaseo, M. DeGiorgi, R. Cingolani, M. Catalano, and P. Crozier, Phys. Rev. B **64**, 125302 (2001).
[45] A. J. Williamson, L. W. Wang, and A. Zunger, Phys. Rev. B **62**, 12963 (2000); C. Y. Ngo, S. F. Yoon, W. J. Fan, and S. J. Chua, *ibid.* **74**, 245331 (2006).